INTERNATIONAL JOURNAL FOR NUMERICAL METHODS IN FLUIDS, VOL. 25, 1263–1284 (1997)

ARBITRARY LAGRANGIAN–EULERIAN MULTICOMPONENT COMPRESSIBLE FLOW WITH FLUID–STRUCTURE INTERACTION

A. SORIA* AND F. CASADEI

European Commission, Safety Technology Institute, Joint Research Centre, I-21020 Ispra, Italy

SUMMARY

The aim of this work is to model the transient dynamic interaction between multicomponent compressible fluid flows and general elastoplastic structures, possibly undergoing large motions and deformations. The fluid domain is treated by a node-centred finite volume method, using an approximate Riemann solver to compute the numerical flux. The use of an arbitrary Lagrangian–Eulerian kinematical description and a non-structured fluid grid is essential for the adopted coupling strategy with the structural domain, which is modelled by finite elements and uses a Lagrangian description. © 1997 John Wiley & Sons, Ltd.

Int. J. Numer. Meth. Fluids, **25**: 1263–1284 (1997)

No. of Figures: 13. No. of Tables: 1. No. of References: 24.

KEY WORDS: compressible fluids; transient dynamics; fluid–structure interaction; arbitrary Lagrangian–Eulerian

1. INTRODUCTION

In the numerical simulation of fast transient dynamic phenomena involving fluid–structure interactions (FSIs), the equilibrium equations for the structural domain are usually formulated in a reference frame which moves simultaneously with the structure (Lagrangian description) and discretized via finite elements (FEs). On the other hand, the analysis of computational fluid dynamics (CFD) problems is normally formulated in a purely Eulerian manner, in which the discretization points are fixed in the reference frame and finite volumes (FVs) are used for the spatial discretization. The study of fluid–structure interactions thus requires the overall description to be formulated in such a manner as to accommodate these two extreme situations.

The fluid domain is considered to be an arbitrary (multicomponent) mixture of inert Joule gases, for which the internal energy is a monotonically increasing function of temperature, and not undergoing any chemical process. However, the possibility of extending the present model to account for reactive flows is taken into account in the selection of the numerical scheme.

The aim of this work is twofold. The first task is to extend some now well-established numerical strategies for the treatment of the CFD problems under consideration from a Eulerian context towards

---

* Correspondence to: A. Soria, Institute for Prospective Technological Studies, World Trade Center Building, Isla de la Cartuja S/N, E-41092 Sevilla, Spain

Contract grant sponsor: STI-JRC/ENELCRIS; Contract grant number: 10399-94-88 T1ED ISP I.

CCC 0271–2091/97/111263–22 $17.50
Received February 1996
Revised February 1997

a more general, arbitrarily moving, non-structured finite element grid by means of an arbitrary Lagrangian–Eulerian (ALE) formulation. The selected numerical scheme is the node-centred finite volume method,[1,2] using an approximate Riemann solver to compute the numerical flux and combined with a MUSCL-like technique to obtain second-order accuracy. The extension of the FV-ALE formulation[3,4] to non-structured grids proposed by Nkonga and Guillard[5] has been considered here, taking into account also quadrangular elements.

The second task is to effectively couple the proposed (FV-based) model for multicomponent flow with general, FE-based models of the structural components, possibly undergoing large displacements, rotations and deformations. These FE models were already available in PLEXIS-3C, a general computer code for transient dynamic analysis of fluid–structure systems being jointly developed, since 1986, by the French Commissariat à l'Energie Atomique (CEN Saclay) and the European Commission (JRC Ispra); see e.g. Reference 6. The ability to perform coupled FSI analyses has been proven essential in many real applications, because the behaviour of the fluid may be strongly influenced by the motion and the response of the solid structure. The implementation of the present multicomponent models in PLEXIS-3C is currently limited to 2D plane analysis,[7] but the extension to other geometric descriptions (axisymmetric, 3D) is under way.

The governing equations for multicomponent compressible inviscid gas flows are given in Section 2. Then in Section 3 the numerical discretizations in time and space of these equations are described. Section 4 presents the technique used for the coupling of the fluid and structural domain descriptions. Finally, several numerical examples illustrating the performance of the method are given.

2. STATEMENT OF PROBLEM

2.1. Conservation equations

The multicomponent Euler equations are to be solved within the fluid domain. Restricting ourselves in two space dimensions, these equations are expressed in conservative form as

$$\partial W/\partial t + \nabla \cdot \mathbf{F}(W) = 0. \tag{1}$$

The *conserved variables* W and the components of the *flux vector* $\mathbf{F} = (F_x, F_y)$ are given by

$$W = \begin{bmatrix} \rho_1 \\ \rho_2 \\ \vdots \\ \rho_\Gamma \\ \rho u \\ \rho v \\ \rho E \end{bmatrix}, \qquad F_x = \begin{bmatrix} \rho_1 u_x \\ \rho_2 u_x \\ \vdots \\ \rho_\Gamma u_x \\ \rho u_x^2 + p \\ \rho u_x u_y \\ (\rho E + p) u_x \end{bmatrix}, \qquad F_y = \begin{bmatrix} \rho_1 u_y \\ \rho_2 u_y \\ \vdots \\ \rho_\Gamma u_y \\ \rho u_x u_y \\ \rho u_y^2 + p \\ (\rho E + p) u_y \end{bmatrix}, \tag{2}$$

where ρ_k represents the partial density of component $k (k = 1, 2, \ldots, \Gamma)$, u_x and u_y are the components of the velocity vector $\mathbf{u}$, E is the total energy per unit mass and ρ is the total density given by $\sum_k \rho_k$.

The total energy E is made up of the internal energy per unit mass, e, and the kinetic energy per unit mass, $\|\mathbf{u}\|^2/2$, i.e. $E = e + \|\mathbf{u}\|^2/2$. The internal energy per unit volume is given by

$$\rho e = \sum_{k=1}^{\Gamma} \rho_k e_k. \tag{3}$$

Assuming a mixture of Joule gases, each component of the mixture has a *temperature state equation* of the form

$$e_k = e_k(T_k), \tag{4}$$

where T_k is the thermodynamic temperature of species k (related to the average kinetic energy of particles from the kth species), thus having $e_k(0) = 0, \forall k$.

Local thermodynamic equilibrium will be assumed, so the thermal field will be characterized by a unique temperature for all components, i.e. $T = T_1 = \cdots = T_\Gamma$ at each spatial location. Assuming a polynomial function of degree n_k for each constitutive relation, we have

$$e_k = \sum_{i=1}^{n_k} C_{ki} T^i. \tag{5}$$

Given a state vector W of conserved variables, equations (3) and (4) allow for the computation (by means of an iterative algorithm if necessary) of the temperature as a function of ρ_k and e_k.

For a mixture of gases with constant heat capacities the temperature is given by

$$T = e/C_\mathrm{v}, \tag{6}$$

where the heat capacity of the mixture at constant volume, C_v, is calculated according to

$$C_\mathrm{v} = \sum_{k=1}^{\Gamma} C_{\mathrm{v}k} \frac{\rho_k}{\rho}. \tag{7}$$

Here $C_{\mathrm{v}k}$ stands for the specific heat at constant volume for component k.

The equation linking the pressure p with the conserved quantities W_i is provided by the following *pressure state equation*, valid for an ideal mixture of Joule gases:

$$p = p(\rho_1, \ldots, \rho_\Gamma, \rho e) = RT \sum_{k=1}^{\Gamma} \frac{\rho_k}{w_k}, \tag{8}$$

where R is the *universal constant of gases* and w_k the *molar mass* of component k. Note that equation (8) is just an expression of Dalton's law of partial pressures. The partial derivatives of pressure with respect to the conserved variables are

$$\kappa = \frac{\partial p}{\partial \rho e} = p \Big/ \left(T \sum_{k=1}^{\Gamma} \rho_k \frac{\mathrm{d}e_k}{\mathrm{d}T} \right), \tag{9}$$

$$\chi_k = \frac{\partial p}{\partial \rho_k} = \frac{RT}{w_k} - \kappa e_k(T). \tag{10}$$

In addition to these derivatives, another important physical property is the *sound speed*, which is given by

$$c = \sqrt{\left(\frac{\partial p}{\partial \rho} \right)_{s, m_k}} = \sqrt{\left(\kappa h + \sum_{k=1}^{\Gamma} \chi_k \frac{\rho_k}{\rho} \right)} = \sqrt{\left((\kappa + 1) \frac{p}{\rho} \right)}, \tag{11}$$

where the partial derivative is computed at constant entropy s and number of moles m_k of each component. The hypothesis of a mixture of Joule gases has been made to obtain the right-hand-side expression, and h denotes the mixture enthalpy per unit mass:

$$h = e + p/\rho. \tag{12}$$

2.2. *Source term and chemistry*

The consideration of the enthalpy of formation for each species, $\Delta h^0_{\mathrm{f},k}$, has been omitted in the expression of the internal energy. It would play a role only in the case where chemical processes were considered when taking into account a *source term* in (1). Although the present work does not consider the presence of source terms, a possible future extension to include this feature has been taken into account when developing the numerical model. In this case, maintaining the assumption of the absence of any diffusive phenomena (viscous effects, thermal conduction or molecular diffusion), the governing equation would be

$$\partial W/\partial t + \nabla \cdot \mathbf{F}(W) = S(W). \tag{13}$$

The source term is given by

$$S(W) = \left(\dot{\rho}_1, \dot{\rho}_2, \ldots, \dot{\rho}_\Gamma, \rho g_x, \rho g_y, \rho \mathbf{g} \cdot \mathbf{u} - \sum_{k=1}^{\Gamma} \Delta h^0_{\mathrm{f},k} \dot{\rho}_k \right)^{\mathrm{T}}, \tag{14}$$

where $\mathbf{g} = (g_x, g_y)$ are the body forces and $\dot{\rho}_k$ is the *local rate of production* of component *k*, which has to be computed from the local chemical composition and the chemical characteristics of the mixture.

2.3. *Hyperbolicity of conservation equations*

Given an arbitrary direction in space defined by two points *i* and *j*, let us denote by $\mathbf{n}_{ij}$ the unit vector normal to this direction. A projection of the flux vector $\mathbf{F}$ onto $\mathbf{n}_{ij}$ can be made, yielding $F_{ij}(W) = \mathbf{F}(W) \cdot \mathbf{n}_{ij}$. The conservation system (1) is known to be hyperbolic, so the Jacobian matrix associated with $F_{ij}(W)$,

$$A_{ij}(W) = \partial F_{ij}(W)/\partial W, \tag{15}$$

can be diagonalized and has real eigenvalues for all physically compatible states for any direction projection $\mathbf{n}_{ij}$. In addition, it can be shown that $F_{ij}(W) = \underset{\sim}{A}_{ij}(W)W$ (Euler identity). A *sufficient condition* for the hyperbolicity of the system is that the pressure equation of state verifies the Euler relationship, i.e.

$$p = \frac{\partial p}{\partial \rho e}\rho e + \sum_{k=1}^{\Gamma} \frac{\partial p}{\partial \rho_k}\rho_k = \kappa \rho e + \sum_{k=1}^{\Gamma} \chi_k \rho_k, \tag{16}$$

as is the case for a mixture of Joule gases.

These properties imply that there exists a set of characteristic variables $U = f(W)$ for which the conservation equation (1) can be decoupled into a system of $\Gamma + 3$ pure advection equations (linear or not) whose advection speeds are the eigenvalues of A_{ij}:

$$\partial U/\partial t + \underset{\sim}{\Lambda} \nabla U = 0, \tag{17}$$

where

$$\underset{\sim}{\Lambda} = \underset{\sim}{T}^{-1} \underset{\sim}{A}_{ij} \underset{\sim}{T} = \mathrm{diag}\{\lambda_1, \ldots, \lambda_1, \lambda_2, \lambda_3\}, \tag{18}$$

with $\lambda_1 = u_n$, $\lambda_2 = u_n + c$ and $\lambda_3 = u_n - c$, *c* being the sound speed associated with the state *W*. The first $\Gamma + 1$ characteristic fields are associated with *convective* waves, whereas the last two are associated with *pressure* waves. The (linearized) passage from conserved to characteristic variables is made by means of a transformation matrix $\underset{\sim}{T}^{-1}$:

$$U = \underset{\sim}{T}^{-1} W. \tag{19}$$

The Jacobian matrix is given by

$$\underset{\sim}{A}_{ij}(W)=\begin{bmatrix} (\delta_{kl}-Y_k)u_n & Y_k\mathbf{n}_{ij} & 0 \\ (\chi_l+\kappa\|\mathbf{u}\|^2/2)\mathbf{n}_{ij}-u_n\mathbf{u} & u_n\underset{\sim}{I}+\mathbf{u}\mathbf{n}_{ij}-\kappa\mathbf{n}_{ij}\mathbf{u} & \kappa\mathbf{n}_{ij} \\ u_n(\chi_l+\kappa\|\mathbf{u}\|^2/2-H) & H\mathbf{n}_{ij}-\kappa u_n\mathbf{u} & (\kappa+1)u_n \end{bmatrix}, \tag{20}$$

where δ_{kl} is the Kronecker symbol, $u_n=\mathbf{u}\cdot\mathbf{n}$ is the velocity projection along the normal, I is the unit tensor, $Y_k=\rho_k/\rho$ is the mass fraction of component k and $H=h+\|\mathbf{u}\|^2/2$. The notation $\mathbf{u}\mathbf{n}_{ij}$ (resp. $\mathbf{n}_{ij}\mathbf{u}$) denotes the diadic product of vectors, i.e. $(\mathbf{u}\mathbf{n}_{ij})_{kl}=u_k n_{ijl}$.

Using the same notation, the transformation matrices are expressed as

$$\underset{\sim}{T}(W)=\begin{bmatrix} \delta_{kl} & 0 & Y_k & Y_k \\ \mathbf{u} & c\mathbf{b}_{ij} & u+c\mathbf{n}_{ij} & \mathbf{u}-c\mathbf{n}_{ij} \\ \|\mathbf{u}\|^2/2-\chi_l/\kappa & c(\mathbf{b}_{ij}\cdot\mathbf{u}) & H+cu_n & H-cu_n \end{bmatrix}, \tag{21}$$

$$\underset{\sim}{T}^{-1}(W)=\frac{1}{c^2}\begin{bmatrix} c^2\delta_{kl}-Y_k(\chi_l+\kappa\|\mathbf{u}\|^2/2) & Y_k\kappa\mathbf{u} & -Y_k\kappa \\ -c(\mathbf{b}_{ij}\cdot\mathbf{u}) & c\mathbf{b}_{ij} & 0 \\ \frac{1}{2}(\chi_l+\kappa\|\mathbf{u}\|^2/2-cu_n) & \frac{1}{2}(c\mathbf{n}_{ij}-\kappa\mathbf{u}) & \kappa/2 \\ \frac{1}{2}(\chi_l+\kappa\|\mathbf{u}\|^2/2+cu_n) & -\frac{1}{2}(c\mathbf{n}_{ij}+\kappa\mathbf{u}) & \kappa/2 \end{bmatrix}, \tag{22}$$

where $\mathbf{b}_{ij}$ is the unit vector orthogonal to $\mathbf{n}_{ij}$, i.e. $\mathbf{b}_{ij}=(n_{ijx},-n_{ijy})$.

The reader is referred to Reference 8 for further details as well as for the extension to the non-equilibrium formulation.

When the sound speed is very large with respect to the flow speed (i.e. low Mach number), an explicit time integration scheme is unable to correctly track the propagation of all signals. The pressure waves associated with the eigenvalues λ_2 and λ_3 propagate very fast across the domain. The *hyperbolic character* of the equations is preserved, but the influence of the pressure waves affects *very rapidly* the entire domain. The correct tracking of the convective signals would require an *implicit* time integration scheme to overcome the severe time step restriction due to the Courant–Friedrichs–Lewy (CFL) condition for the fast sonic waves.

However, for the kind of applications under consideration (fluid–structure interaction and fast transient phenomena), pressure waves are of major relevance. According to this, an *explicit* time integration scheme seems more adequate to treat the equations within the computational domain. The way in which this time integration scheme is accommodated with the explicit scheme used for the integration of the equilibrium equations in the solid (Lagrangian) domain will be described below.

3. TIME AND SPACE DISCRETIZATION

3.1. Arbitrary Langrangian–Eulerian formulation

The numerical discretization of the conservation equations has been carried out by means of a non-structured finite volume formulation, fully compatible with standard finite element grids. Three-noded triangles and four-noded quadrangles have been considered. The arbitrary Lagrangian–Eulerian method presented here is based on the Godunov scheme[3,9] as recently reformulated in unstructured 3D moving domains by Nkonga and Guillard.[5]

The computational domain will be assumed to be divided into non-overlapping node-centred control volumes delimited by the medians of triangles and quadrangles as shown in Figure 1. The

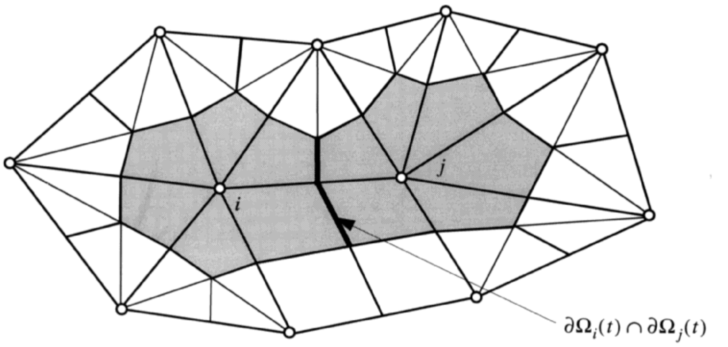

Figure 1. Node-centred control volumes Ω_i and Ω_j

simultaneous use of triangles and quadrangles to construct the node-centred control volumes has been discussed in Reference 10, where several techniques to treat the quadrangles are presented and compared.

We will assume that each grid point is moving with respect to the fixed co-ordinate system with a velocity field $\mathbf{v}(\mathbf{x})$. The conservation equation (1) can be integrated on the moving control volume Ω_i, whose boundary will be denoted by $\partial\Omega_i$. The total rate of change of the conserved quantity within the moving control volume is given by Reynolds' transport theorem:

$$\frac{\mathrm{d}}{\mathrm{d}t}\int_{\Omega_i(t)} W\,\mathrm{d}\Omega_i = \int_{\Omega_i(t)} \left(\frac{\partial W}{\partial t} + \nabla\cdot(W\mathbf{v})\right)\mathrm{d}\Omega_i = \int_{\Omega_i(t)} \frac{\partial W}{\partial t}\,\mathrm{d}\Omega_i + \int_{\partial\Omega_i(t)} [W(\mathbf{v}\cdot\mathbf{n})]\,\mathrm{d}\Upsilon_i, \tag{23}$$

where $\mathrm{d}\Upsilon_i$ is an element of the control volume boundary $\partial\Omega_i(t)$.

Note that Green's theorem has been applied to obtain the last equation, where $\mathbf{n}=\mathbf{n}(t)$ is the normal unit vector to the boundary $\partial\Omega_i(t)$ (outwardly oriented).

Integration between $t=t_n$ and $t=t_n+\Delta t$ yields

$$\int_{\Omega_i(t_n+\Delta t)} W\,\mathrm{d}\Omega_i - \int_{\Omega_i(t)} W\,\mathrm{d}\Omega_i = \int_{t_n}^{t_n+\Delta t}\int_{\Omega_i(t)} \frac{\partial W}{\partial t}\,\mathrm{d}\Omega_i\,\mathrm{d}t + \int_{t_n}^{t_n+\Delta t}\int_{\partial\Omega_i(t)} [W(\mathbf{v}\cdot\mathbf{n})]\,\mathrm{d}\Upsilon_i\,\mathrm{d}t. \tag{24}$$

Let us denote by W_i^n the set of discrete variables approximating the solution of the continuous problem. The quantity W_i^n is then defined as the averaged value of the conserved variable W within the control volume Ω_i at time $t=t_n$:

$$W_i^n = \left(\int_{\Omega_i(t)} W\,\mathrm{d}\Omega_i\right)\Big/|\Omega_i|^n, \tag{25}$$

where $|\Omega_i|^n$ represents the measure (area in two space dimensions) of the control volume Ω_i at time $t=t_n$. Using equation (1), we have

$$|\Omega_i|^{n+1}W_i^{n+1} - |\Omega_i|^n W_i^n = \int_{t_n}^{t_n}\int_{\partial\Omega_i(t)} [W(\mathbf{v}\cdot\mathbf{n})]\,\mathrm{d}\Upsilon_i\,\mathrm{d}t - \int_{t_n}^{t_n+\Delta t}\int_{\Omega_i(t)} [\nabla\cdot\mathbf{F}(W)]\,\mathrm{d}\Omega_i\,\mathrm{d}t. \tag{26}$$

Application of Green's theorem yields

$$|\Omega_i|^{n+1}W_i^{n+1} - \||\Omega_i|^n W_i^n = \int_{t_n}^{t_n+\Delta t}\int_{\partial\Omega_i(t)} [W)\mathbf{v}\cdot\mathbf{n})]\,\mathrm{d}\Upsilon_i\,\mathrm{d}t - \int_{t_n}^{t_n+\Delta t}\int_{\partial\Omega_i(t)} [\mathbf{F}(W)\cdot\mathbf{n}]\,\mathrm{d}\Upsilon_i\,\mathrm{d}t. \tag{27}$$

The time-averaged normal (outwardly oriented) vector corresponding to the portion of the boundary $\partial\Omega_i(t)$ between Ω_i and Ω_j will be denoted as

$$\mathbf{N}_{ij} = \frac{1}{\Delta t}\int_{t_n}^{t_n+\Delta t}\int_{\partial\Omega_i(t)\cap\partial\Omega_j(t)} \mathbf{n}(t)\,\mathrm{d}\Upsilon_i\,\mathrm{d}t, \tag{28}$$

whereas the time-averaged normal velocity of the control volume boundary will be represented as

$$v_{Nij} = \frac{1}{\Delta t\|\mathbf{N}_{ij}\|}\int_{t_n}^{t_n+\Delta t}\int_{\partial\Omega_i(t)\cap\partial\Omega_j(t)} \mathbf{v}(t)\cdot\mathbf{n}(t)\,\mathrm{d}\Upsilon_i\,\mathrm{d}t. \tag{29}$$

Accordingly to these definitions, a discrete version of (27) is given by

$$|\Omega_i|^{n+1}W_i^{n+1} - |\Omega_i|^n W_i^n = \Delta t\sum_{j\in V(i)}\|\mathbf{N}_{ij}\|(W_{ij}v_{Nij} - \Phi_{ij}), \tag{30}$$

where W_{ij} is the *averaged value* on the boundary $\partial\Omega_i(t)\cap\partial\Omega_j(t)$ and from $t = t_n$ to $t = t_n + \Delta t$ of the conserved quantity W and Φ_{ij} is the *averaged numerical flux* between $\partial\Omega_i(t)$ and $\partial\Omega_j(t)$ upon the same time interval and control volume interface. The sum is extended to $V(i)$, which is the set of nodes surrounding node i.

The *numerical flux* Φ_{ij} approximates the term

$$\Phi_{ij} \approx \frac{1}{\|\mathbf{N}_{ij}\|\Delta t}\int_{t_n}^{t_n+\Delta t}\int_{\partial\Omega_i(t)\cap\partial\Omega_j(t)} \mathbf{F}(t)\cdot\mathbf{n}(t)\,\mathrm{d}\Upsilon_i\,\mathrm{d}t \approx f_{\mathrm{A}}(\mathbf{F}(W_i(t^*))\cdot\bar{\mathbf{n}}_{ij}, \mathbf{F}(W_j(t^*))\cdot\bar{\mathbf{n}}_{ij}), \tag{31}$$

where $\bar{\mathbf{n}}_{ij} = \mathbf{N}_{ij}/\|\mathbf{N}_{ij}\|$ is the normalized average vector, $f_{\mathrm{A}}(x, y)$ is an *averaging function* and t^* is a time point between $t = t_n$ and $t = t_n + \Delta t$. The overall order of approximation of the scheme depends on the accuracy of the approximation of these terms in space and time. A method of first-order accuracy in space and time will be presented first. In a subsequent step the extension to second-order accuracy in the space and time variables will be outlined.

Before discussing these issues, it is worthwhile to remark that the conservation principle given by (3) is valid if we take the function $W \equiv 1$ and the corresponding Euler flux $F \equiv 0$. In this case the equation represents an expression of the *conservation of volume* during the grid movement process:

$$|\Omega_i|^{n+1} - |\Omega_i|^n = \Delta t\sum_{j\in V(i)}(v_{Nij}\|\mathbf{N}_{ij}\|). \tag{32}$$

Needless to say, the verification of (32) is a *necessary* condition for the overall numerical conservation scheme to work properly. This can be ensured by computing the mid-step configuration using the arbitrarily prescribed grid displacement nodal velocities and thus calculating the mid-step unit normal vector $\mathbf{N}_{ij}$ according to this configuration. Assuming constant grid velocities for each node within the time interval $[t_n, t_n + \Delta t]$, the time-averaged normal velocity given by (29) can be approximated as

$$v_{Nij} = \frac{1}{\Delta t\|\mathbf{N}_{ij}\|}\left(\frac{\mathbf{v}_{\mathrm{A}} + \mathbf{v}_{\mathrm{B}}}{2}\right)\cdot\int_{t_n}^{t_n+\Delta t}\mathbf{n}(t)\,\mathrm{d}t = \left(\frac{\mathbf{v}_{\mathrm{A}} + \mathbf{v}_{\mathrm{B}}}{2}\right)\cdot\frac{\mathbf{N}_{ij}}{\|\mathbf{N}_{ij}\|} = \left(\frac{\mathbf{v}_{\mathrm{A}} + \mathbf{v}_{\mathrm{B}}}{2}\right)\cdot\bar{\mathbf{n}}_{ij}. \tag{33}$$

where $\mathbf{v}_{\mathrm{A}}$ and $\mathbf{v}_{\mathrm{B}}$ are the velocities corresponding to the points A and B defining each segment of the control volume boundary.

The validity of this approximation depends on the algorithm selected to prescribe the grid motion as well as on the time step size. For grid mappings that are smooth enough, these formulae perform reasonably well and equation (32) is respected. The numerical testing of the volume conservation in the whole domain is advisable in order to detect loss of conservation (even if using a *conservative* formulation) due either to the wrong selection of grid motion or to the loss of validity of the described integration scheme.

3.2. Numerical flux computation: Roe's scheme

One of the popular and efficient methods to carry out the evaluation of the upwind numerical flux for the Euler equations of gas dynamics is Roe's scheme. Like the Godunov method, the scheme is based on *the solution of a Riemann problem* defined by two half-spaces filled with gas at states W_i and W_j, separated by an interface defined by the orthogonal vector $\mathbf{n}_{ij}$. The initial discontinuity (which in general does *not* satisfy the Rankine–Hugoniot conditions) breaks into three generic discontinuities *compatible* with the above-mentioned conditions, travelling at different speeds. The method proposed by Godunov is based on the *exact solution* of the Riemann problem, which requires an iterative procedure, whereas the Roe scheme is based on an *approximate solution* of the Riemann problem, which is less expensive from the computational standpoint. The extension of Roe's approximate Riemann solver to moving grids can be made by following the techniques proposed by Harten and Hyman[4] for the monodimensional case and by Nkonga and Guillard[5] for the multidimensional case.

It is well known that the *exact solution to the Riemann problem* defined by W_i, W_j and $\mathbf{n}_{ij}$ (denoted W^{R}) is self-similar, i.e. $W^{\mathrm{R}}(x, t, W_i, W_j) = W^{\mathrm{R}}((x/t), W_i, W_j)$, where the co-ordinate x is measured along the direction of $\mathbf{n}_{ij}$. The Godunov numerical flux is then given by

$$\Phi(W_i, W_j, \mathbf{n}_{ij}) = \mathbf{F}(W^{\mathrm{R}}(0, W_i, W_j)) \cdot \mathbf{n}_{ij}. \tag{34}$$

In other words, the Godunov numerical flux is given by the mathematical flux projected onto the direction $\mathbf{n}_{ij}$ particularized for the state vector solution of the corresponding Riemann problem at the point $x = 0$, i.e. at the position of the original interface.

In order to avoid the iterative solution at each control volume interface of the associated Riemann problem, Roe proposed the use of an *approximate Riemann solver*. The reader is referred to Reference 11 for theoretical details on this numerical scheme. Here the approach provided by Abgrall[12] and Liu and Vinokur[8] has been followed. The *Roe numerical flux* between two states W_i and W_j projected along a direction is given by

$$\Phi(W_i, W_j, \mathbf{n}_{ij}) = \tfrac{1}{2}[\mathbf{F}(W_i) \cdot \mathbf{n}_{ij} + \mathbf{F}(W_j) \cdot \mathbf{n}_{ij}] + \tfrac{1}{2}|\tilde{\mathbf{A}}(W_i, W_j, \mathbf{n}_{ij})|(W_i - W_j), \tag{35}$$

where $\mathbf{F}(W_i) \cdot \mathbf{n}_{ij}$ is the mathematical flux corresponding to the state W_i projected along the direction $\mathbf{n}_{ij}$ and $\tilde{A}(W_i, W_j, \mathbf{n})$ is the so-called *Roe-averaged Jacobian matrix*. For the single-component Euler equations it can be shown that there exists an *average state* $\tilde{W}$ such that $\utilde{A}_{ij}(W_i, W_j) = \utilde{A}(\tilde{W})$. However, this property is *lost* for the general multicomponent case. The Roe-averaged Jacobian matrix is *not* uniquely defined. The velocity, mass fractions and total enthalpy are averaged according to the general formula

$$\tilde{M} = \frac{\sqrt{\rho_i} M_i + \sqrt{\rho_j} M}{\sqrt{\rho_i} + \sqrt{\rho_j}}, \tag{36}$$

where M generically denotes one of these quantities. The averages $\tilde{\kappa}$ and $\tilde{\chi}_k$ are defined in such a way as to fulfil the pressure jump condition

$$\Delta p = \tilde{\kappa}\Delta(\rho e) + \sum_{k=1}^{\Gamma} \tilde{\chi}_k \Delta\rho_k, \tag{37}$$

where $\Delta a = a_i - a_j$ for each variable. Several ways have been proposed to compute the averaged quantities $\tilde{\kappa}$ and $\tilde{\chi}_k$. The approach followed here is the one described in Reference 12, to which the reader is referred for further details.

It has been observed that the use of the correction to the multicomponent Roe scheme proposed by Larrouturou[13] becomes mandatory to ensure the positiveness of the mass fractions. This correction consists basically of upwinding all the partial densities according to the sign of the total mass numerical flux.

The classical scheme accounts for the flux crossing a Eulerian interface $\partial\Omega_i \cap \partial\Omega_j$. To extend this to the more general case in which the interface moves with a normal velocity v_{Nij}, a simple Lagrangian transport term has to be added, thus yielding the following expression for the Roe numerical flux:

$$\Phi(W_i, W_j, \mathbf{n}_{ij}) = \tfrac{1}{2}\{[\mathbf{F}(W_i) + \mathbf{F}(W_j)] \cdot \mathbf{n}_{ij} - v_{Nij}(W_i + W_j) + |\tilde{\mathbf{A}}(W_i, W_j, \mathbf{n}_{ij}) - v_{Nij}\mathbf{I}|(W_i - W_j)\}. \quad (38)$$

3.3. *Extension to second order*

The consideration of the second-order scheme is based on a MUSCL-like extrapolation applied to the above-presented first-order scheme. The extension of van Leer's monodimensional, finite difference method[16] to the multidimensional case based on unstructured finite volumes[1,2] has provided satisfactory results also when combined with Roe's approximate Riemann solver or with other numerical flux schemes.[15,16]

If an estimate of the gradient of the variables is available, the cell-constant representation of the variables can be replaced by a linear representation around the same cell-averaged value, thus allowing for better estimates of the primitive variables at the cell boundaries, where the flux contributions are to be computed according to (38). The procedure is illustrated in Figure 2, where a cut on the line joining two cells is shown. The second-order fluxes are obtained using the extrapolated variables on the boundary, W_{ij} and W_{ji}, rather than the cell-averaged primitive variables W_i and W_j:[17]

$$\begin{bmatrix} W_{ij} = W_i + \nabla W_i \cdot (\mathbf{x}_{(i+j)/2} - \mathbf{x}_i) \\ W_{ji} = W_j + \nabla W_j \cdot (\mathbf{x}_{(i+j/2)} - \mathbf{x}_j) \end{bmatrix}, \quad (39)$$

where $\mathbf{x}_{(i+j)/2}$ is the position of the interface between control volumes and *not* the midpoint between nodes i and j.

Since the conserved discrete variables are node-centred, the construction of an element-centred set of gradients is straightforward. Assuming a linear (or bilinear) representation of the variables within the element, a set of node-centred values of the gradient can then be obtained by averaging elemental

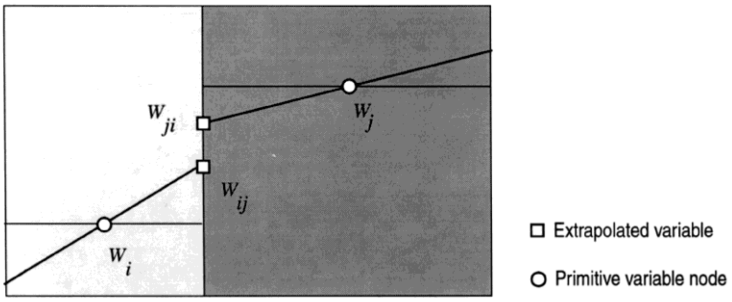

Figure 2. Spatial second-order flux evaluation

contributions. Denoting by $T(i)$ the set of elements sharing node i, a discrete approximation for the gradient of a generic variable W in the node-centred control volume Ω_i can be estimated as

$$\nabla W_i = \left(\sum_{j \in T(i)} \nabla W_j |T(i) \cap \Omega_i| \right) \Big/ |\Omega_i|. \tag{40}$$

Nevertheless, the use of the exact gradients in the calculation of the boundary-extrapolated variables leads to non-physical oscillations in the solution in the vicinity of a discontinuity (or steep gradient). To remedy this, a *local gradient limitation* is required. Equation (40) is replaced in practice by

$$\nabla W_i = \text{minmod}\ (\nabla W_j), \quad j \in T(i). \tag{41}$$

Recall that the minmod operator is defined as

$$\text{minmod}\ (a_1, \ldots, a_n) = \begin{cases} \text{sgn}(a_1) \min(|a_1|, \ldots, |a_n|) & \text{if sgn}\ (a_1) = \cdots = \text{sgn}\ (a_n), \\ 0 & \text{otherwise.} \end{cases} \tag{42}$$

A spatially second-order-accurate scheme is then obtained from (38) by replacing W_i and W_j by W_{ij} and W_{ji} respectively as given by (39):

$$\begin{aligned} \Phi(W_{ij}, W_{ji}, \mathbf{n}_{ij}) = \tfrac{1}{2}\{&[\mathbf{F}(W_{ij}) + \mathbf{F}(W_{ji})] \cdot \mathbf{n}_{ij} - v_{Nij}(W_{ij} + W_{ji}) \\ &+ |\tilde{\underset{\sim}{A}}(W_{ij}, W_{ji}, \mathbf{n}_{ij}) - v_{Nij}\, \underset{\sim}{I}|(W_{ij} - W_{ji})\}. \end{aligned} \tag{43}$$

Second-order accuracy in time can be obtained with a two-step procedure combined with the preceding MUSCL spatial interpolation. The reader is referred to Reference 14 for an outline of the original finite difference method and to Reference 1 or 2 for details concerning its extension to the unstructured finite volume format.

4. FLUID–STRUCTURE NUMERICAL COUPLING

4.1. Structural dynamics equations: integration algorithm

The multicomponent fluid dynamics model described in the preceding sections has to be coupled with a general structural dynamics finite element model. The spatial discretization adopted in the PLEXIS-3C code is based on the finite element formulation of the equilibrium equations. These equations are typically expressed within structural elements using a Lagrangian scheme. The nodes of structural elements thus typically follow the motion of material particles and no flow of mass is considered across structural element interfaces. The elemental deformation process induces *elemental internal stresses* according to the *constitutive law* of the material under consideration. These elemental stresses are projected (by spatial integration) onto the nodes, as is customary within the finite element method, thus yielding a set of equivalent *internal nodal forces*:

$$\mathbf{f}_{\text{int},i} = \sum_{j \in L(i)} \int_{\Xi_j} \mathbf{B}_j^{\mathrm{T}} \underset{\sim}{\sigma}_j \, \mathrm{d}\Xi_j, \tag{44}$$

where $L(i)$ is the set of elements including node i, $\mathbf{B}_j$ and σ_j are the elemental shape function derivative matrix and the elemental Cauchy stresses corresponding to element j respectively and Ξ_j is the element volume in the current configuration. The summation operator indicates a standard finite element assembly procedure. In addition to these internal forces, external forces $\mathbf{f}_{\text{ext},i}$ are assumed to be applied to the solid (body forces or externally applied loads). The reaction forces arising from imposed essential boundary conditions and, in particular, the interaction forces acting from a fluid in contact with the structure are considered among these external forces, as will be shown in the next subsection. Directly specified external forces can be simply prescribed as natural boundary conditions.

The nodal masses M_i are obtained by spatial integration in a similar manner: the *consistent mass matrix* obtained by integration of classical finite element shape functions is reduced to *diagonal form*, in which each entry represents the corresponding nodal mass, by means of the row-sum mass-lumping technique.

Having made the spatial discretization of the equilibrium equations, a semidiscrete form of Newton's law reads

$$M_i \dot{\mathbf{u}}_i = \mathbf{f}_{\text{ext},i} - \mathbf{f}_{\text{int},i}, \tag{45}$$

where $\mathbf{u}_i$ is the nodal velocity. Since nodal displacements are the basic unknowns within a Lagrangian formulation, the first-order equation (45) is usually expressed as

$$M_i \ddot{\mathbf{d}}_i = \mathbf{f}_{\text{ext},i} - \mathbf{f}_{\text{int},i}, \tag{46}$$

where $\mathbf{d}_i$ are the nodal displacements. The sign criterion assumes that the external force induces the solid deformation, whereas the internal force is the restoring one.

The *central difference method* is used to perform the time integration of this second-order equation. This scheme is usually written as

$$\begin{aligned} \mathbf{u}^{n+1} &= \mathbf{u}^n + \frac{\Delta t}{2}(\dot{\mathbf{u}}^n + \dot{\mathbf{u}}^{n+1}), \\ \mathbf{d}^{n+1} &= \mathbf{d}^n + \Delta t\left(\mathbf{u}^n + \frac{\Delta t}{2}\dot{\mathbf{u}}^n\right), \end{aligned} \tag{47}$$

where $\mathbf{d}$ is the vector of nodal displacements, $\mathbf{u}$ is the vector of nodal velocities, $\dot{\mathbf{u}}$ is the vector of accelerations, the upper suffix n denotes a quantity at time t^n and $n+1$ denotes a quantity at time $t^{n+1} = t^n + \Delta t$.

The integration scheme (47) for the structural domain is implemented as follows in PLEXIS-3C. Assume that a complete solution, i.e. all discretized quantities (displacements $\mathbf{d}$, velocities $\mathbf{u}$, accelerations $\dot{\mathbf{u}}$, stresses $\underset{\sim}{\sigma}$ and related variables) are known at time t^n. First an intermediate (half-step) velocity is introduced,

$$\bar{\mathbf{u}}^{n+1/2} = \mathbf{u}^n + \frac{\Delta t}{2}\dot{\mathbf{u}}^n, \tag{48}$$

which is denoted $\bar{\mathbf{u}}$ in order to stress the difference from $\mathbf{u}$. This is the constant velocity that would transform configuration n into configuration $n+1$ over a time interval Δt in the discretization process. From the second equation of (47) the new displacements are given by

$$\mathbf{d}^{n+1} = \mathbf{d}^n + \Delta t \bar{\mathbf{u}}^{n+1/2}. \tag{49}$$

On this new configuration the stress $\underset{\sim}{\sigma}^{n+1}$ can now be evaluated by application of the constitutive relations. Then the new field of accelerations $\dot{\mathbf{u}}^{n+1}$ can be directly computed via the discretized equilibrium equations (45) and finally the new velocities are obtained from the first equation of (47).

It is important to note that in the time integration process the new configuration induced by the displacements $\mathbf{d}^{n+1}$ is obtained first (at the initial time the configuration is known by definition), then equilibrium is applied *on the current configuration*, while the velocities $\mathbf{u}^{n+1}$ corresponding to this new configuration are computed only at the end of the time-stepping procedure.

Note that this time integration scheme is explicit in that all quantities in the right-hand-side terms are known when the equations are applied, thus no system solver is required.

4.2. Fluid–structure interaction modelling

The interaction between the fluid and the solid structure can be modelled in PLEXIS-3C thanks to a numerical technique based on the Lagrange multiplier method.[18,19] The boundary conditions for moving solid walls for the fluid domain are directly concerned by this issue, so a short outline of the method will be given here for the sake of completeness.

The basic interaction scheme for *permanent* fluid–structure contact (see definition below) is illustrated in Figure 3. The fluid-structure interface is discretized by a double series of nodes connected by a one-to-one relation. The motion of the structural nodes in the interface is Lagrangian, whereas the interface nodes from the fluid side are ALE and their motion constantly follows that of the corresponding structural nodes.

The task of the grid-rezoning technique within the bulk of the fluid domain consists of updating the configuration of 'internal' fluid nodes so as to respect the movement of any Lagrangian interfaces (in particular, of the structure), by simultaneously minimizing the grid distortion. Various remeshing algorithms are presently implemented in PLEXIS-3C and there exists also a user routine by means of which the analyst can prescribe a custom rezoning law. However, for the test cases presented here, extensive use of the default automatic rezoning technique has been made. The reader is referred to Reference 20 for details on this numerical technique.

The kinematic boundary condition $\mathbf{u} \cdot \mathbf{n}_{ij} = 0$ has to be taken into consideration for the fluid node. The boundary condition can be imposed on a *weak manner* by integrating the numerical flux across an interface lying on a wall, moving with normal velocity v_N:

$$\Phi^{\mathrm{SW}}(W_{\mathrm{nb}}, \mathbf{n}_{ij}) = \int_{\partial\Omega_{\mathrm{nb}}\cap\partial\Omega} p_{\mathrm{nb}}[0 \ \ldots \ 0 \ n_{ijx} \ n_{ijy} \ v_N]^{\mathrm{T}} \, \mathrm{d}\sigma, \tag{50}$$

where $\partial\Omega_{\mathrm{nb}}$ denotes the boundary of the control volume centred around the boundary node and $\partial\Omega$ represents the boundary of the whole computational domain. This technique has been successfully used in applications with no fluid–structure interaction. In particular, a for Eulerian solid boundary (rigid wall) the above equation can be used by simply taking $v_N = 0$. Note that the integration of the numerical flux given by (50) does *not* ensure a zero normal velocity for the boundary node.

For fluid-structure interaction problems a key point is to ensure that the fluid node and the linked structural node maintain exactly the same normal velocity, so the wall boundary condition has to be computed in a *strong manner*. The fluid experiences a reaction force **r** (momentum flux) exactly equal to the opposite of the action made by the fluid onto the structure. The appropriate way to compute this *reaction force* will be described below. Note that, according to the central difference time integration scheme, the reaction **r** has to be computed at time $t = t^n$. Since the configuration $\mathbf{x}^n$ is known, a

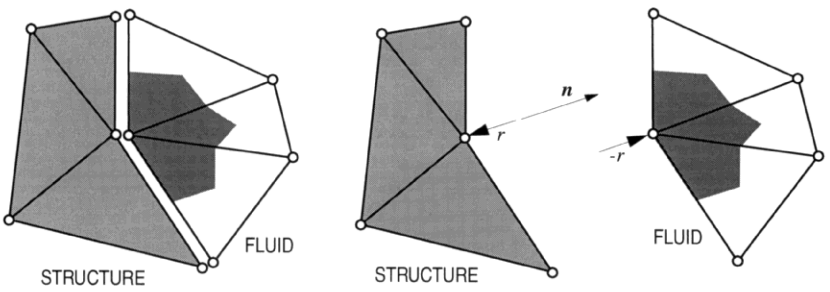

Figure 3. Discretization of fluid–structure interface

geometrical estimate of the normal $\mathbf{n}^n$ in (51) can be made (the reader is referred to Reference 19 for further details on this issue).

The interaction problem is numerically decoupled by finding the interaction forces $\mathbf{r}$ acting on each interface code and by considering them separately according to the action–reaction principle applied to the respective fluid or structural node. For an *inviscid fluid*, $\mathbf{r}$ is directed *along the normal* $\mathbf{n}$ to the interface and is computed by imposing that the components of the fluid and structure velocities ($\mathbf{u}_\mathrm{F}$ and $\mathbf{u}_\mathrm{S}$) along $\mathbf{n}$ have to be identical, so as to avoid fluid detachment or superposition (*permanent contact*):

$$\mathbf{u}_\mathrm{F}\cdot\mathbf{n}-\mathbf{u}_\mathrm{S}\cdot\mathbf{n}=n_x^n u_{\mathrm{F},x}^n+n_y^n u_{\mathrm{F},y}^n-n_x^n u_{\mathrm{S},x}^n-n_y^n u_{\mathrm{S},y}^n=0. \tag{51}$$

Similar constraints (linking the motion of two or more nodes) can be established for a number of kinematic degrees of freedom of the overall system. These generalized constraints can be represented as a set of n_k equations (equal to the number of kinematic constraints)

$$\mathbf{C}\mathbf{u}^n=\mathbf{b}, \tag{52}$$

where $\mathbf{C}$ is an $n_k\times m_k$ matrix (whose coefficients are the normal vector components) and m_k is the *subset* of kinematic degrees of freedom of the system subjected to constraints. Owing to its generality, this approach can be used to impose arbitrary linear links among any kinematic degrees of freedom of the problem.

On the other hand, the equilibrium equation *for the subset of constrained degrees of freedom* is expressed by means of the $m_k\times m_k$ system of equations (recall that this system is diagonal since the mass-lumping technique is used)

$$\mathbf{M}^n\dot{\mathbf{u}}^n=\mathbf{f}_\mathrm{ext}^n-\mathbf{f}_\mathrm{int}^n+\mathbf{r}^n. \tag{53}$$

Using the integration scheme $\mathbf{u}^n=\bar{\mathbf{u}}^{n-1/2}+\Delta t_n\dot{\mathbf{u}}^n/2$, equation (52) can be expressed as a function of the acceleration as

$$\mathbf{C}\dot{\mathbf{u}}^n=\frac{2}{\Delta t_n}(\mathbf{b}-\mathbf{C}\bar{\mathbf{u}}^{n-1/2})=\mathbf{s}. \tag{54}$$

The m_k unknown reactions can be generically expressed as a function of the n_k Lagrange multipliers $\underset{\sim}{\lambda}$ as

$$\mathbf{r}=\mathbf{C}^\mathrm{T}\underset{\sim}{\lambda}. \tag{55}$$

Substituting (55) into (53), these relations can be merged into the expression

$$\begin{bmatrix}\mathbf{C} & \mathbf{O}\\ \mathbf{M}^n & -\mathbf{C}^\mathrm{T}\end{bmatrix}\begin{bmatrix}\dot{\mathbf{u}}^n\\ \lambda\end{bmatrix}=\begin{bmatrix}\mathbf{s}\\ \mathbf{f}_\mathrm{ext}^n-\mathbf{f}_\mathrm{int}^n\end{bmatrix}. \tag{56}$$

The solution of this system of equations formally provides the accelerations of the constrained nodes as well as the Lagrange multipliers which allow the computation of the reactions at the fluid–structure interface. In practice, however, the Lagrangian multipliers and thus the reactions are computed first, then these are added to the prescribed external forces and finally all accelerations are obtained via the general equilibrium equation (45).

Having obtained the reactions, the solid wall boundary condition is imposed in a *strong* manner by

$$\Phi^\mathrm{SW}(W_\mathrm{nb},\mathbf{n}_{ij})=\left[0\ \ldots\ 0,\mathbf{r}_x,\mathbf{r}_y,\int_{\partial\Omega_\mathrm{nb}\cap\partial\Omega}p_\mathrm{nb}v_N\,\mathrm{d}\sigma\right]^\mathrm{T}. \tag{57}$$

Note that the energy flux is still computed in a weak manner. According to our preliminary results, this approach seems to yield better performance.

5. NUMERICAL EXAMPLES

5.1. *Shock tube computations*

The shock tube test is a well-known problem extensively used for the assessment of numerical methods in the analysis of compressible flows. The test consists of the solution of a single Riemann problem. A tube is divided into two parts separated by a membrane. The gas (single-component in this case) filling the left and right half-spaces is initially at states W_L and W_R respectively. At time $t = 0$ the membrane is assumed to break and the initial discontinuity (not satisfying the Rankine–Hugoniot conditions) breaks into *three* characteristics discontinuities (shock wave, contact discontinuity and rarefaction wave) travelling at different speeds. The tests presented in this section correspond to the set of initial data proposed in the benchmark exercise carried out by Sod:[21] $\rho_L = 1$, $p_L = 1, u_L = 0$ and $\rho_R = 0{\cdot}125, p_R = 0{\cdot}1, u_R = 0$ respectively. The universal constant of gases, the

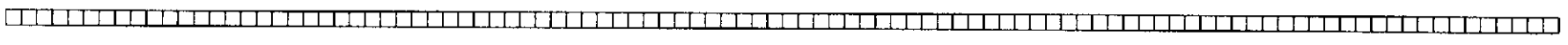

100 quadrilateral elements

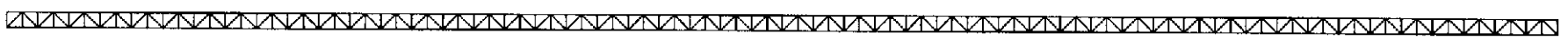

200 triangular elements

a)

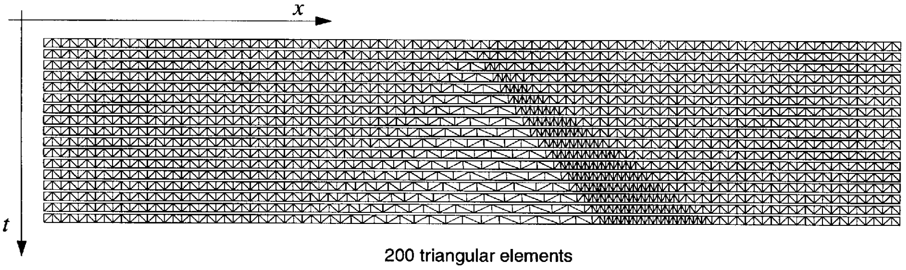

200 triangular elements

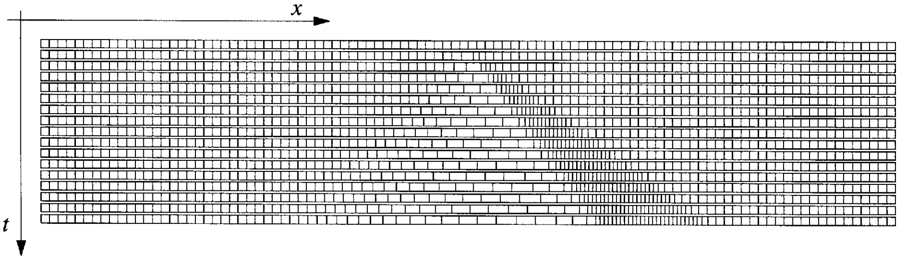

100 quadrilateral elements

b)

Figure 4. Sod shock tube: computational grids and deformed Lagrangian meshes

specific heat and the molar weight are selected so as to yield $\gamma = 1{\cdot}4$. The computations have been done using both quadrangular and triangular elements with the grids shown in Figure 4(a). All calculations have been carried out using a time-stepping procedure so as to have the minimum grid Courant number $Co = [(|u| + c)\Delta t]/(\Delta x)_{\rm ch}$ equal to 0·5, $(\Delta x)_{\rm ch}$ being the characteristic 'diameter' of each element.

A first series of computations has been done on a Eulerian frame. A comparison has been made among the results obtained with the first- and second-order schemes using either triangles or quadrangles.

The results obtained with the *first-order* scheme using both triangles and quadrangles are compared in Figure 5(a) with the exact solution. The shock wave is captured slightly better than the contact discontinuity wave in all figures, since the time step selection is made on the basis of the Courant number for the fastest signal ($u + c$). No difference is observed in the sharpness of the discontinuities obtained using triangles or quadrangles, but a significant advantage in the capture of the rarefaction fan tail is noted when quadrangles are used.

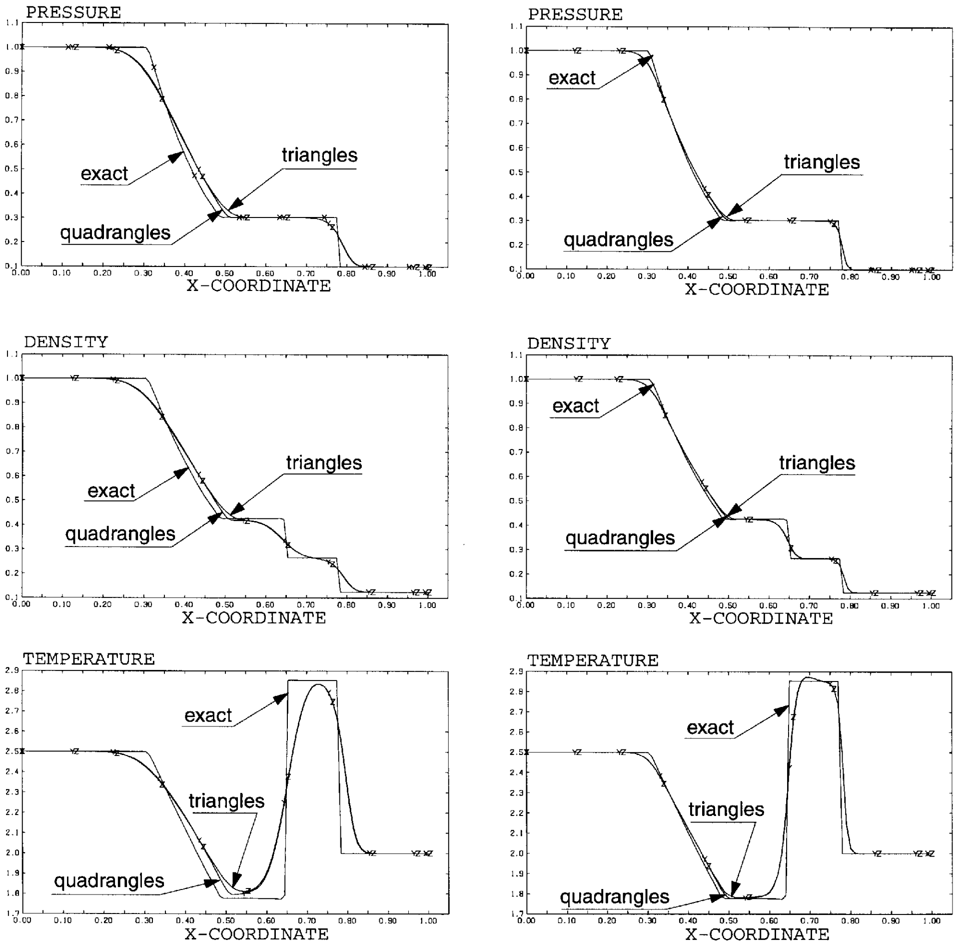

a) first-order solutions

b) second-order solutions

Figure 5. Sod shock tube: Eulerian solutions

Figure 5(b) illustrates the results obtained with the *second-order* scheme. The solution quality is noticeably improved. Note also that the differences between the results obtained with triangles and those obtained with quadrangles are less important than in the first-order case.

The same shock tube problem has then been analysed using a fully Lagrangian formulation, prescribing each node in the grid to move *with the velocity of the particles*. The algorithm testing on this frame is important because a correct solution necessarily precludes the appearance of (strong) velocity oscillations (otherwise the node motion would produce elements with negative area). The transient is illustrated in Figure 4(b), which shows the evolution of the computational grid as the transient proceeds up to $t = 0{\cdot}16$ s for both types of elements. Notice the regularity of the grid compression between the shock and the contact discontinuity as well as the uniform widening of the element size in the rarefaction fan zone.

Figure 6(a) shows the *first-order* solution at $t = 0{\cdot}16$ s for pressure, density and temperature. The tracking of the shock wave is better than the one obtained in the Eulerian calculation, but a noticeable numerical oscillation follows the contact discontinuity development. This defect is particularly

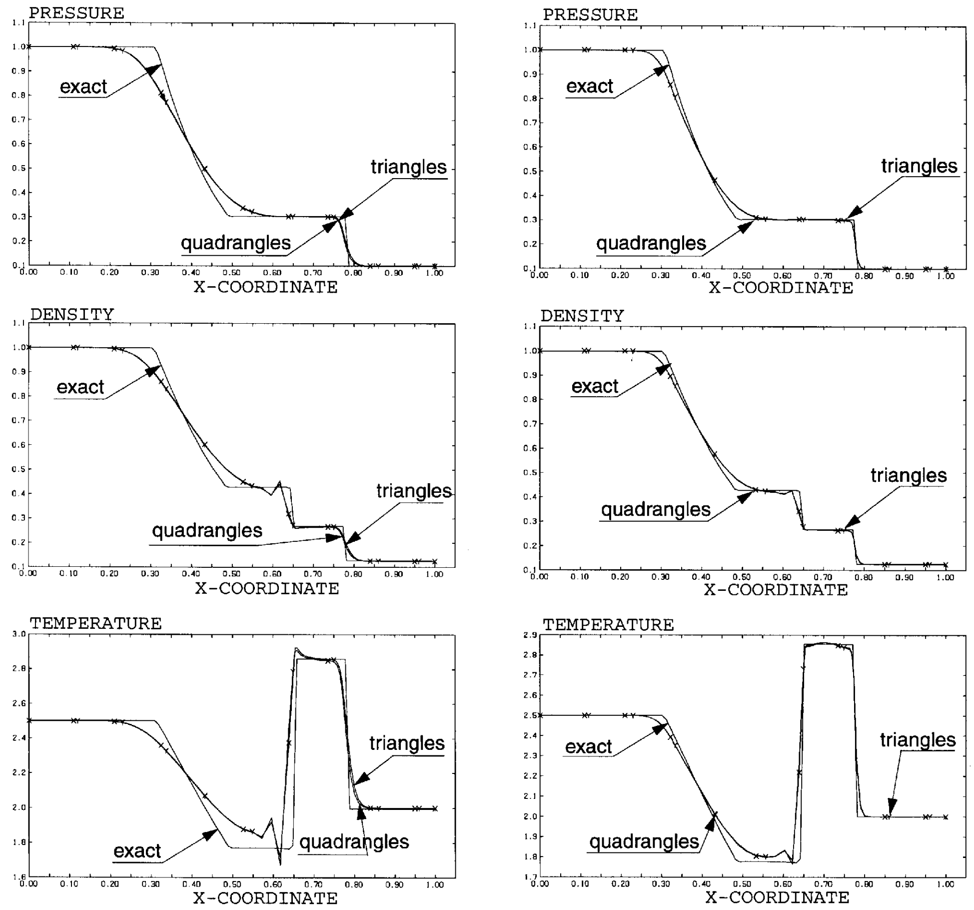

a) first-order solutions

b) second-order solutions

Figure 6. Sod shock tube: Lagrangian solutions

evident in the temperature field plot, where a certain delay of the temperature peak is also observed with respect to the exact solution.

The results for the *second-order* Lagrangian computation are shown in Figure 6(b). Here again the shock sharpness is greater than the one corresponding to the Eulerian computation. The appealing improvement of this solution with respect to the first-order Lagrangian computation is better observed in the density and temperature fields, where the oscillations following the contact discontinuity almost disappear and the temperature peak fits remarkably well the exact solution.

Note also that the first-order solutions obtained with triangles and quadrangles are almost identical in the rarefaction fan tail, the main differences being concentrated between the shock and the contact discontinuity. For second-order computations the use of triangles or quadrangles produces indistinguishing results.

5.2. Two-component shock tube

The first test problem involving actual multicomponent flow concerns a shock tube problem with two components and aims at assessing the correctness of the scheme under these circumstances. The problem data have been taken from Reference 13. The shock tube is divided into two equal zones separated by a membrane that breaks at $t = 0$, thus initiating the transient. The left zone contains a pure perfect gas (A) with $\gamma_A = 1{\cdot}4$ at a state defined by $p_A = 1, \rho_A = 1$, whereas the right zone contains another pure perfect gas (B) with $\gamma_B = 1{\cdot}2$ at a state defined by $p_B = 0{\cdot}1$, $\rho_B = 0{\cdot}125$. The test is a two-component version of the classical Sod problem analysed in Section 5.1. The computations have been done using a Eulerian 100×1 quadrangle grid (as in Figure 4(a), top).

The solution pattern is very similar to the one corresponding to the Sod problem, although the three intermediate states separated by the characteristic waves are different (owing to the different values of γ for the two gases). The mass of gas A advances with the contact discontinuity, compressing gas B, where the typical shock wave develops.

Figure 7 summarizes the results obtained with the first- and second-order schemes and either the Eulerian or the Lagrangian formulations for several fields (pressure, temperature, total density, mass fraction of component A and velocity) at $t = 0{\cdot}16$. As pointed out by Larrouturou,[13] the modification of the Roe solver to perform the upwinding of the partial density fluxes is mandatory to preserve the positivity of the scheme. These results agree also with those presented by Ruel.[22]

5.3. Shock diffraction by a deformable ring

This test aims at simulating the effect of a blast wave on a ring placed in the middle of a wind tunnel. The test has been taken from Reference 22, where it was analysed by assuming fixed wall boundaries (rigid ring) and using a purely Eulerian formulation. Some changes in the problem data have been made in order to formulate the problem according to the real values of the physical (dimensional) quantities.

The computational domain is sketched in Figure 8. The fluid domain ABCD is initially at rest, with $p = 0{\cdot}1$ MPa and $T = 300$ K. The fluid is assumed to be a perfect gas (specific heat ratio $\gamma = 1{\cdot}4$, molecular weight $w = 28{\cdot}96, c_v = 20{,}780\,\mathrm{J\,kmol^{-1}\,K^{-1}}$). The universal constant of gases is $R = 8312\,\mathrm{J\,kmol^{-1}\,K^{-1}}$. A shock wave enters the channel at time $t = 0$ through the lower open boundary AB. The shock is characterized by the upwind state $p_{ext} = 0{\cdot}4$ MPa, $T_{ext} = 480$ K, $\mathbf{u}_{ext} = (0, 311{\cdot}28)\,\mathrm{m\,s^{-1}}$, satisfying the Rankine–Hugoniot conditions. The shock Mach number is $Ma_{ext} = 0{\cdot}896$.

The shock interacts with the cylindrical shell structure depicted in Figure 8. The shell material is a steel which is assumed to behave as an elastoplastic material characterized by the following

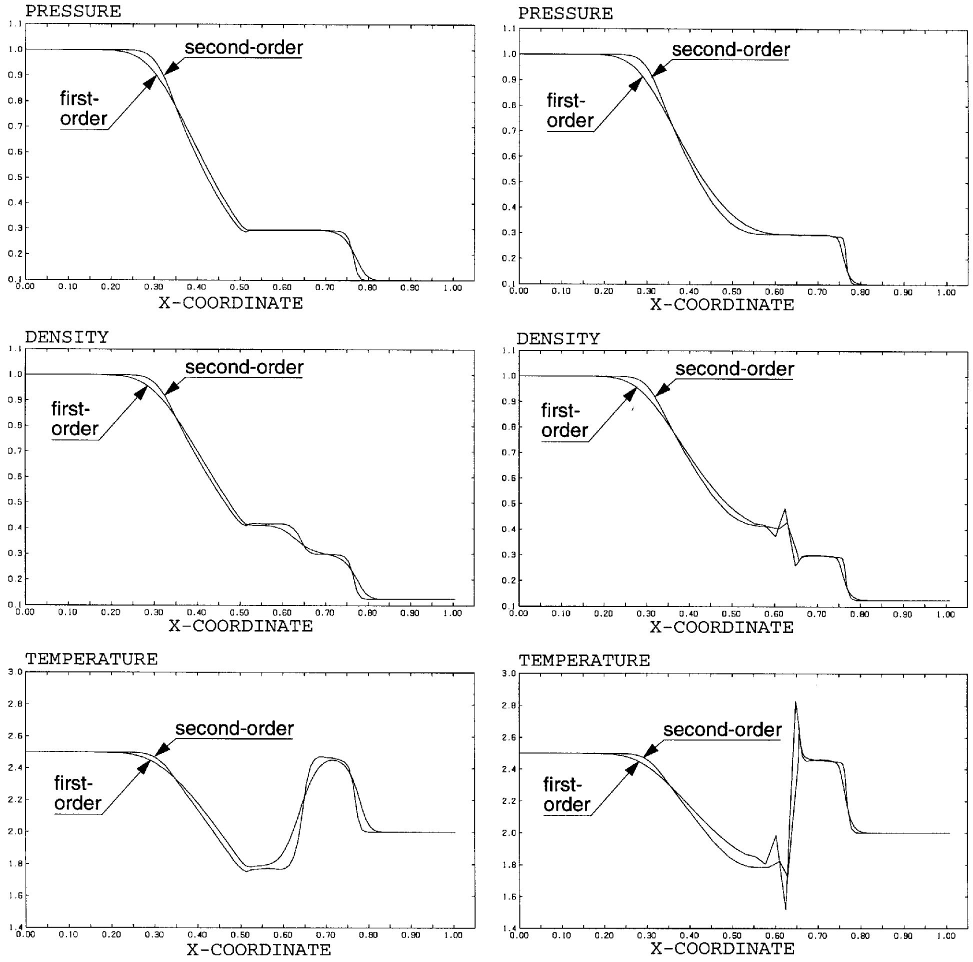

a) Eulerian solutions b) Lagrangian solutions

Figure 7. Two-component shock tube: Eulerian and Lagrangian solutions

constitutive properties: density 7800 kg m^{-3}, Young modulus $1{\cdot}6\times10^{11}$ Pa, Poisson ratio 0·333, elastic limit $1{\cdot}05\times10^{8}$ Pa, plastic slope $1{\cdot}6\times10^{10}$ Pa. The shell thickness is 0·12 cm.

The boundary conditions for sides AD and BC are those corresponding to a solid wall, whereas the far-field condition on the open boundary DC corresponds to the initial gas state. The structure is blocked at point E opposite the shock incidence point. The analysed transient covers up to $t=3$ ms.

The pressure field at three selected times is displayed in Plate 1(a). Plate 1(b) shows the temperature field, Plate 1(c) the density field and Plate 1(d) the velocity fields. The calculation is merely demonstrative of the mechanical response of the steel shell to the impact of the blast wave, since no other results are available for comparison.

Concerning the solution obtained in the fluid domain, the computed fields qualitatively agree fairly well with the numerical results presented by Godunov *et al.*[3] (using a first-order-accurate, exact

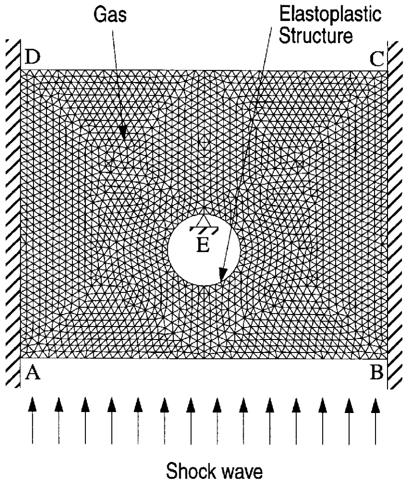

Figure 8. Shock diffraction by a deformable ring: problem definition

Riemann solver numerical scheme) and Ruel[22] (using a second-order-accurate Hänel–van Leer scheme). A reflected shock appears and two symmetric supersonic zones develop behind the shell.

5.4. *Supersonic flow over a deformable step*

This problem has also become a classical test to assess numerical schemes for compressible flows.[7,22–24] The supersonic flow over a step was analysed in the mentioned references by assuming rigid walls and by using a purely Eulerian formulation. In this test the step created in the channel at time $t=0$ will be assumed to be made up of a material flexible enough to undergo a relatively large deformation.

The test definition is sketched in Figure 9. The channel length is 3 m and its height is 1 m. A perfect gas is flowing at Mach 3 speed. The gas is assumed to have $\gamma = 1{\cdot}4$, $w=28{\cdot}96$ and $c_v = 20{,}780\,\mathrm{J\,kmol^{-1}\,K^{-1}}$. The universal constant of gases is $R=8312\,\mathrm{J\,kmol^{-1}\,K^{-1}}$. The Mach 3 flow is characterized by $p_0 = 0{\cdot}3$ MPa, $\mathbf{u}=(1202.73,\ 0)\,\mathrm{m\,s^{-1}}$ and $T=400$ K.

At time $t=0$ an obstacle 0·2 m high appears at a distance 0·6 m from the tunnel inlet. This obstacle is assumed to be made of steel, behaving as an elastoplastic material whose properties are the same as in the previous example (Section 5.3). The steel shell is assumed to be 2 cm thick and has been modelled using the same two-noded shell elements that have been employed in the preceding examples.

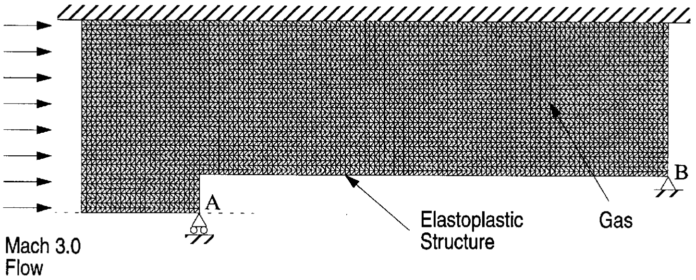

Figure 9. Supersonic flow over a deformable step: problem definition

The produced shock hits the steel structure, distorting its initial shape according to the mechanical boundary conditions applied. For the computation presented here, it has been assumed that the point B has its three degrees of freedom (x-displacement, y-displacement and rotation) blocked, whereas the point A has its y-displacement blocked. The transient analysed covers up to 3·5 ms.

The transient on the pressure field is illustrated in Plate 2(a). The numerical solution obtained for the steel shell deformation has not been compared with any other results. The computed pressure field within the fluid sufficiently far from the deformable step agrees very well with the results published in the above-mentioned references for the rigid step case. Note that the angle of the second shock reflection (which takes place on the shell surface) is markedly smaller than what is observed in the rigid step case. This is due to the convex-shaped deformation undergone by the horizontal part of the structure close to the step wedge during the transient.

The transient results for the temperature are shown in Plate 2(b). Plate 2(c) shows the density field at the three selected time points and Plate 2(d) shows the velocity fields.

5.5. Explosion in a vessel

This last test is merely demonstrative and aims at showing the capabilities of the model in handling applications similar to those encountered in safety engineering. In the fluid–structure problems presented in the above subsections, the flow as *external* to the structure. This case deals with an *internal* flow case: an explosion inside a container produces a significant deformation in the tank walls. The scope from the engineering standpoint would be to investigate the critical conditions that make the vessel shell collapse.

The geometrical characteristics of the problem are sketched in Figure 10. The upper part of the flat tank is initially filled with air, whereas the bottom part contains a heavier gas (argon), both of them at an initial pressure $p_{\mathrm{air}} = p_{\mathrm{A}} = 0{\cdot}1$ MPa. A bubble of hydrogen at high pressure $p_{\mathrm{H}} = 2{\cdot}5$ MPa is also assumed to be present at the initial time. The initial temperature $T_{\mathrm{air}} = T_{\mathrm{A}} = T_{\mathrm{H}} = 300\,\mathrm{K}$ is uniform inside the container. The universal constant of gases is $R = 8312\,\mathrm{J\,kmol^{-1}\,K^{-1}}$. The other gas properties are summarized in Table I.

The vessel is made of steel, which is assumed to behave as an elastoplastic material characterized by the same properties used in the example of Section 5.3. The assumed shell thickness is 1·5 mm and the shell structure is blocked at points A and B (see Figure 10).

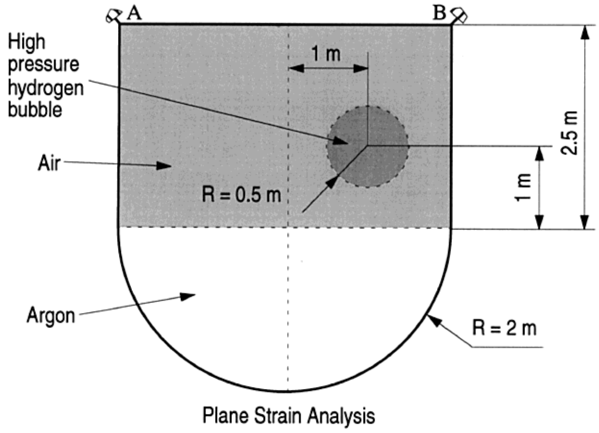

Figure 10. Explosion in a vessel: problem definition

Table I

Property	Hydrogen	Air	Argon
Specific heat ratio γ	1·4	1·4	1·269
Molecular weight w (kg kmol^{-1})	2	28·96	40
Specific heat c_v (J kmol^{-1} K^{-1})	20780	20780	30900

The transient will be analysed up to $t = 2$ ms. The computational results are illustrated by plotting some selected scalar fields at times $t = 0{\cdot}5$, 1, 1·5 and 2 ms. The deformation undergone by the vessel is large enough to be noticed without a deformation amplification factor (especially at the final time).

The pressure transient is outlined in Plate 3(a). The estimated overpressure reached in the neighbourhood of point B is about 3.2 MPa at time $t = 1{\cdot}5$ ms. The evolution of the temperature field is shown in Plate 3(b), while Plate 3(c) shows the evolution of the air mass fraction. The dynamics of the explosion is illustrated in Plate 3(d), where a plot of the velocity field at the selected times has been made. The expanding shock first reaches the vertical, right-hand part of the vessel and only somewhat later the upper side. The reflected shocks interact with the expanding blast wave, producing a complex flow pattern.

6. CONCLUSIONS

A new model for the treatment of multicomponent compressible flows has been implemented in PLEXIS-3C. It is based on a node-centred finite volume approach which uses the underlying finite element mesh (made up of either triangles or quadrangles) to construct the conservation cells. The computation of the numerical flux among these cells is made by means of an approximate Riemann solver technique. The grid motion, necessary to accommodate the Lagrangian (or material) formulation for the structures with the typical Eulerian (or spatial) formulation in the fluid, has been handled by means of an arbitrary Lagrangian–Eulerian technique. The combination of these new models with the existing fluid–structure interaction algorithm takes carefully into account the characteristics of the time-integration schemes used for the solid and fluid domains respectively and ensures a strong coupling at the fluid–structure interface.

A set of benchmark exercises has been produced to assess the performance of the method for both purely Eulerian and ALE computations.

ACKNOWLEDGEMENTS

The present activity has been partly supported by Third Party Work contract 10399-94-88 T1ED ISP I between the Safety Technology Institute (STI) of the Joint Research Centre (JRC) and ENELCRIS.

REFERENCES

1. A. Dervieux, ‘Steady Euler simulations using unstructured meshes’, *VKI Lect. Ser. 1984–04*, 1985.
2. L. Fezoui, ‘Résolution des équations d’Euler par un schéma de Van Leer en éléments finis’, *INRIA Rep. 358*, Unité de Recherche INRIA-Sophia Antipolis, 1985.
3. S. Godunov, A. Zabrodin, M. Ivanov, A. Kraiko and G. Prokopov, *Résolution Numérique des Problèmes Multi-dimensionnels de la Dynamique des Gaz*, MIR, Moscow, 1979 (Russian 1st edn 1976).
4. A. Harten and J. M. Hyman, ‘Self adjusting grid methods for one-dimensional hyperbolic conservation laws’, *J. Comput. Phys.*, **50**, 115–173 (1984).
5. B. Nkonga and H. Guillard, ‘Godunov-type method on non-structured meshes for three-dimensional moving boundary problems’, *Comput. Methods Appl. Mech. Eng.*, **113**, 183–204 (1994).

6. H. Bung, F. Casadei, J. P. Halleux and M. Lepareaux, 'PLEXIS-3C: a computer code for fast dynamic problems in structures and fluids', *Proc. 10th Int. Conf. Structural Mechanics in Reactor Technology, SMiRT-10*, Anaheim, CA, August 1989.
7. A. Soria and F. Casadei, 'Modelling of arbitrary Lagrangian–Eulerian multicomponent flow with fluid–structure interaction in PLEXIS-3C', *JRC Spec. Publ. I.95.01*, 1995.
8. Y. Liu and M. Vinokur, 'Nonequilibrium flow computations. I. An analysis of numerical formulations of conservation laws', *J. Comput. Phys.*, **83**, 373–397 (1989).
9. S. Godunov, 'A difference scheme for numerical computation of discontinuous solutions of equations of fluid dynamics', *Math. Sb.*, **47**, 271–290 (1959).
10. V. Selmin, 'The node-centered finite volume approach: bridge between finite differences and finite elements', *Comput. Methods Appl. Mech. Eng.*, **102**, 107–138 (1993).
11. P. L. Roe, 'Approximate Riemann solvers, parameter vectors and difference schemes', *J. Comput. Phys.*, **43**, 357–372 (1981).
12. R. Abgrall, 'Généralisation du schéma de Roe pour le calcul d'écoulements de mélanges de gaz à concentration variable', *Rech. Aérosp*, **6**, 31–43 (1988).
13. B. Larrouturou, 'How to preserve the mass fractions positivity when computing multicomponent flows', *J. Comput. Phys.*, **95**, 59–84 (1991).
14. B. van Leer, 'Towards the ultimate conservative difference scheme (II). Monotonicity and conservation combined in a second order scheme', *J. Comput. Phys.*, **14**, 361–370 (1974).
15. G. Fernandez, 'Implicit conservative upwind schemes for strongly transient flows', *INRIA Rep. 873*, Unité de Recherche INRIA-Sophia Antipolis, 1988.
16. D. Chargy, R. Abgrall, L. Fezoui and B. Larrouturou, 'Comparisons of several upwind schemes for multicomponent one-dimensional inviscid flows', *INRIA Rep. 1253*, Unité de Recherche INRIA-Sophia Antipolis, 1990.
17. B. van Leer, 'Towards the ultimate conservative difference scheme (V). A second-order sequel to Godunov's method', *J. Comput. Phys.*, **32**, 101–136 (1979).
18. M. Lepareux, B. Schwab, A. Hoffmann, P. Jamet and H. Bung, 'Un programme général pour l'analyse dynamique rapide—cas des tuyauteries', *Colloq.: Tendances Actuelles en Calcul des Structures*, Bastia, November 1985.
19. F. Casadei and J. P. Halleux, 'On the treatment of fluid–structure interactions of the permanent type in PLEXIS-3C', *Proc. Second Int. Conf. on Computational Structures Technology*, Athens, August–September 1994.
20. S. Giuliani, 'An algorithm for continuous rezoning of the hydrodynamic grid in arbitrary Lagrangian–Eulerian computer codes', *Nucl. Eng. Des.*, **72**, 205–212 (1982).
21. G. A. Sod, 'A survey of several finite difference methods for systems of nonlinear hyperbolic conservation laws', *J. Comput. Phys.*, **27**, 1–31 (1978).
22. F. Ruel, 'Numerical simulation of reacting gas flows: assessment calculations of transonic multidimensional flows', *Joint Research Centre Tech. Note I.92.01*, 1992.
23. P. Woodward and P. Colella, 'The numerical simulation of two dimensional fluid flow with strong shocks', *J. Comput. Phys.*, **54**, 115–173 (1984).
24. T. Buffard and J. M. Herard, 'Méthodes de résolution pour les systèmes hyperboliques en forme conservative sur maillage structuré et non structuré. Rapport d'avancement 2', *Note. Tech. HE-41/91.26A*, Electricité de France, Direction des Etudes et Recherches, Département LNH, 1991.